Earth, Planets and Space

EXPRESS LETTER

Open Access

A numerical model for precursory time sequences of the phreatic eruptions of Mt. Ontake, central Japan

Yuta Maeda[1*]

Abstract

The 2014 phreatic eruption of Mt. Ontake was preceded by increased volcano-tectonic (VT) seismicity, but all other types of precursors were obscure. A subsurface process leading to eruption with few precursors has yet to be identified. This study performed numerical simulations to reproduce the precursory time sequence of the eruption. High-temperature water from a cooling magma reservoir was injected into a modeled porous medium filled with cold water. This resulted in an immediate pressure increase and a delayed temperature increase in the shallow parts. The pressure increased immediately because the injected fluid pushed the existing fluid away from the porous medium. A sharp boundary between low (initial)- and high (injected)-temperature regions, known as a thermal front, developed and migrated upward slowly, leading to a delayed temperature increase. The lag time between the pressure and temperature changes is likely responsible for the precursory VT seismicity. If the injected water temperature was less than the critical point, the water was liquid throughout the model region until the thermal front reached a shallow part, where the pressure was low enough for the heated water to vaporize. This vaporization was sudden and large, likely leading to a large eruption with few precursors, similar to the time sequence in 2014. If the injected water temperature was higher, the water volume increased gradually from liquid to supercritical and then to the gas state. This scenario likely led to a small eruption with numerous precursors, similar to the previous eruption of Mt. Ontake that occurred in 2007.

*Correspondence:
Yuta Maeda
maeda@seis.nagoya-u.ac.jp
Full list of author information is available at the end of the article

Graphical Abstract

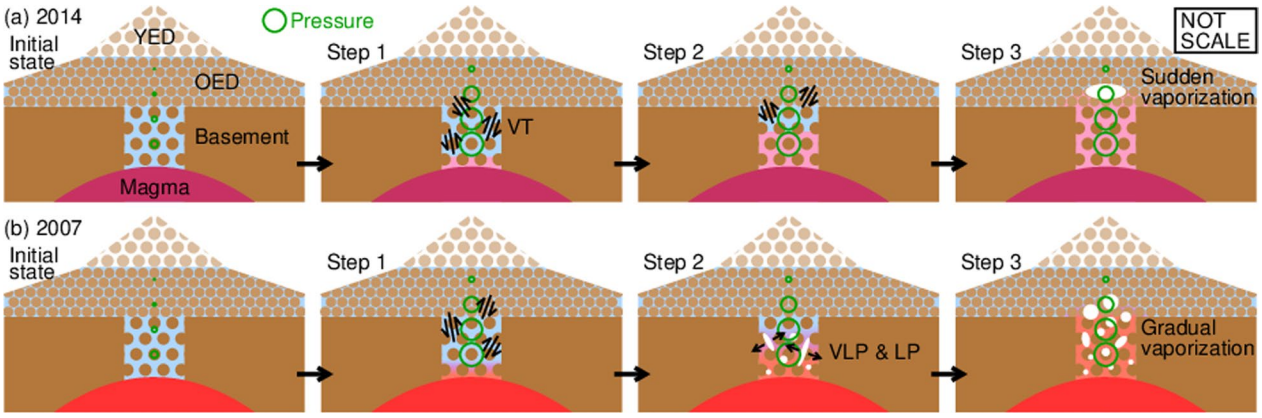

Introduction

The phreatic eruption of Mt. Ontake, central Japan, on September 27, 2014, led to 63 victims and missing persons. The significant damage was primarily due to almost no precursors. The Japan Meteorological Agency (JMA) and Nagoya University noticed volcano-tectonic (VT) seismicity that started at the end of August, 2014, and peaked on September 11, with 85 earthquakes a day (JMA 2014). This was the only clear precursor that provided sufficient lead time to issue a warning; no volcanic tremor, no crustal deformation, a normal plume height ($\leq$ 300 m), and only five long-period (LP) events during September 14–24, 2014, were associated with this crisis until ~ 10 min before the eruption (JMA 2014). Several other precursors were identified after the eruption using special techniques. Kato et al. (2015) applied a matched filter technique and identified > 20 small LP events that peaked at September 15–16, 2014, and were hidden in continuous seismograms. Terakawa et al. (2016) investigated the focal mechanisms of VT earthquakes and suggested that the local stress field in the summit region of Mt. Ontake deviated from the regional stress field before the 2014 eruption probably because of an injection of fluids into this region. Miyaoka and Takagi (2016) identified a slight crustal deformation during the ~ 1 month before the eruption, which was recognized only after stacking the baselines of 3–4 station pairs. These studies indicated the presence of LP and crustal deformation precursors, but they were too weak to be recognized by normal monitoring approaches.

Precursors were more prominent before the previous eruption of Mt. Ontake, which occurred in late March 2007 (Nakamichi et al. 2009). The first precursor was a VT swarm that began in December 2006. Crustal deformation, which was attributed to magma intrusion into shallow parts (Nakamichi et al. 2009; Takagi and Onizawa 2016; Murase et al. 2016), was observed during the same period. A very long period (VLP) seismic event followed on January 25, 2007, that was large enough to be recognized at distances of > 20 km. Afterward, the VT seismicity decreased, while the LP seismicity increased and reached a maximum of > 40 events per day in early March. Abundant volcanic tremors occurred during this period (Nakamichi et al. 2009).

Despite more prominent precursors in 2007 than in 2014, the eruption size was larger in 2014. The 2007 eruption produced a thin ashfall in a limited (100–200 m) region around a crater (JMA 2007). The volcano explosivity index (VEI; Newhall and Self 1982) was 0. The 2014 eruption expelled ballistic blocks to ~ 1 km, a pyroclastic density current to ~ 3 km, and ashfall to several tens of kilometers. The total volume of the ejected materials was $0.7 - 1.3 \times 10^6 m^3$ (Maeno et al. 2016), and the corresponding VEI was 2.

Although numerous studies have addressed the 2014 eruption by seismological (Kato et al. 2015; Maeda et al. 2015, 2017; Ogiso et al. 2015; Terakawa et al. 2016), geodetic (Takagi and Onizawa 2016; Murase et al. 2016; Miyaoka and Takagi 2016), geochemical (Sano et al. 2015), geological (Ikehata and Maruoka 2016; Maeno et al. 2016; Oikawa et al. 2016; Miyagi et al. 2020), and modeling (Tsunematsu et al. 2016) approaches, the subsurface process leading to the 2014 eruption with few precursors has yet to be identified. This study addressed this issue using numerical modeling of fluid

and heat flows in a hydrothermal system beneath Mt. Ontake.

Method

This study computed spatiotemporal evolutions of the pore-fluid pressure and temperature in a water-saturated porous medium induced by the injection of hot water at the bottom of the medium (Fig. 1). Although recent numerical simulations of hydrothermal systems tend to use multicomponent fluids (e.g., Tanaka et al. 2018; Stissi et al. 2021; Arens et al. 2022), this study considered pure water because it aimed to deduce the fundamentals for understanding the 2014 eruption with minimum complexity rather than introducing many parameters that were not satisfactorily constrained by observations. The considered trigger for phreatic eruptions was a sudden increase in water volume, typically due to a phase transition from liquid to gas. For the first-order approximation, liquid water was assumed for the initial state because this study focused on the preeruption period.

The model was solved at three complexity levels. First, a one-dimensional (1-D) model (Fig. 1a) was solved analytically, where constant fluid properties were assumed. It showed several key features of the response of a hydrothermal system to hot fluid injection. Second, realistic fluid properties were introduced into the 1-D model. It was solved numerically, and the key features deduced from the analytical solution were examined in case of the realistic fluid properties. Third, a realistic geometry was introduced as a two-dimensional (2-D) axi-symmetric model (Fig. 1b) that approximated the shallow subsurface of Mt. Ontake. This was the most realistic model used in this study. The 2-D simulation results were interpreted based on the features derived from the 1-D analytical and numerical models. This three-step approach was more effective than performing only the 2-D simulation in understanding the results.

The 1-D analytical model was solved for the region from $z = -L$ to $z = 0$ (Fig. 1a), where z is the vertical coordinate (positive: upward). The basic equations are the conservation of mass:

$$\frac{\partial \rho_f}{\partial t} = -\frac{1}{\phi}\frac{\partial (\rho_f V)}{\partial z}, \tag{1}$$

Darcy's law:

$$V = -\frac{k}{\mu_f}\left(\frac{\partial P}{\partial z} + \rho_f g\right), \tag{2}$$

and the conservation of energy (Woods 2015):

$$\frac{\partial T}{\partial t} = -V_T\frac{\partial T}{\partial z} + D_T\frac{\partial^2 T}{\partial z^2}, \tag{3}$$

$$V_T = \frac{\rho_f C_{pf}}{\phi\rho_f C_{pf} + (1-\phi)\rho_s C_{ps}}V, \tag{4}$$

$$D_T = \frac{\phi K_f + (1-\phi)K_s}{\phi\rho_f C_{pf} + (1-\phi)\rho_s C_{ps}}, \tag{5}$$

where t is time; ϕ and k are the porosity and permeability of the porous medium, respectively; g is the gravitational acceleration; ρ is the density; C_p is the isobaric heat capacity; and K is the thermal conductivity. The subscripts f and s denote the quantities for fluid and solid, respectively. Equation (3) has the form of an advection–diffusion equation, with the apparent advection velocity and diffusion constant given by V_T and D_T, respectively. The Darcy velocity V, temperature T, and pressure P are the dependent variables to be solved. The remaining quantities are treated as constants in the analytical solution. Equations (1)–(5) constitute 1-D versions of the equations described by Woods (2015).

The 1-D numerical model used the same geometry as the analytical model (Fig. 1a), with $L = 1.2$ km; ρ_f, μ_f, C_{pf}, and K_f were given as functions of pressure

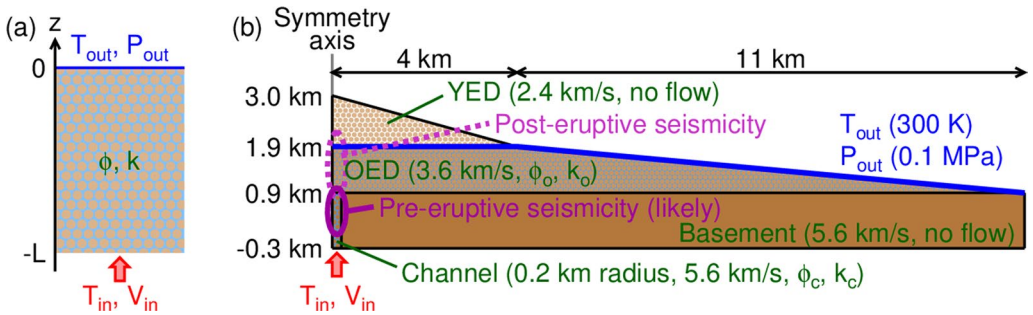

Fig. 1 Configurations of (**a**) one-dimensional and (**b**) two-dimensional models

and temperature based on the industrial formulation 1997 (IF-97) developed by the International Association for the Properties of Water and Steam (IAPWS). It was valid over 273.15–1073.15 K for ≤ 100 MPa and 1073.15–2273.15 K for ≤ 50 MPa (COMSOL 1998–2022a). The simulation used typical values for volcanic rock properties (Heap et al. 2020):

$$\phi = 0.05, \tag{6}$$

$$\rho_s = 2500 \mathrm{kgm}^{-3}, \tag{7}$$

$$C_{ps} = 800 \mathrm{Jkg}^{-1}\mathrm{K}^{-1}, \tag{8}$$

and

$$K_s = 1 \mathrm{Wm}^{-1}\mathrm{K}^{-1}. \tag{9}$$

The 2-D model (Fig. 1b) consisted of younger (< 0.1 Ma) and older (0.78–0.39 Ma) eruptive deposit layers (YED and OED, respectively) underlain by the basement; their spatial extents were based on the results of a seismic structural survey (Maeda and Watanabe 2023). Hot water was injected at 0.3 km below sea level (bsl.), where the roof of a cooling magma reservoir was estimated to be present (Maeda and Watanabe 2023). A permeable flow channel with a 0.2 km radius was assumed to be present through the basement layer (Fig. 1b) based on a 0.4-km-wide subvertical seismicity that was attributed to upward fluid migration from the reservoir (Maeda and Watanabe 2023). The seismicity was distributed through the OED layer during the study period of 2017–2021 of Maeda and Watanabe (2023) but was ~ 1 km deeper before the 2014 eruption (Kato et al. 2015), suggesting that the migration stopped near the bottom of the OED before the eruption (Fig. 1b). Maeda and Watanabe (2023) postulated that the OED acts as a barrier to upward fluid migration. This study modeled the barrier using a smaller porosity (ϕ_o) and permeability (k_o) in the OED than in the channel (ϕ_c and k_c). Note that forbidding the flow in the OED ($k_o = 0$) resulted in almost no flow over the entire region; a new fluid could enter the porous medium only if the existing fluid that had filled the medium could escape. Therefore, a small but nonzero k_o value was assumed. The fluid and heat flows were computed only in the channel and OED for simplicity. The outlet of the flow was placed along the top of the OED (blue line in Fig. 1b); the YED was considered unsaturated based on Asai et al. (2006), who proposed a groundwater flow along the YED–OED boundary. A crustal deformation caused by the elevated pore fluid pressure was computed on an approximated topographical surface (Fig. 1b). A poroelasticity model was used, in which the pore fluid pressure change multiplied by the Biot-Willis coefficient (α_B) acted as the deformation source (COMSOL 1998–2022b). To stabilize the calculation, the fluid and heat flows were first computed, and the results were then used to compute the deformation (one-way coupling). Therefore, α_B did not influence the fluid or heat flow.

All simulations used the following boundary conditions (Fig. 1): a temperature T_{out} and a pressure P_{out} at the outlet, a temperature T_{in} ($> T_{out}$) and a Darcy velocity V_{in} at the inlet, and no mass and heat fluxes across the other boundaries. The initial conditions were a temperature T_{out} and zero Darcy velocity (hydrostatic equilibrium). A finite element method was implemented using COMSOL Multiphysics software. See Additional file 1 for exact numerical procedures and parameters.

Results

1-D analytical model

Equations (1)–(5) were solved analytically by assuming a constant fluid density ρ_f, which is a good approximation for liquid water. Letting $\partial\rho_f/\partial t = 0$ and $\partial\rho_f/\partial z = 0$ in Eq. (1) results in $\partial V/\partial z = 0$, and thus $V = V_{in}$. Inserting this result into (2) yields

$$\frac{\partial P}{\partial z} = -\rho_f g - \frac{\mu_f V_{in}}{k}. \tag{10}$$

The first term on the right-hand side of this equation indicates a hydrostatic pressure gradient. The second term represents the increase in the pressure gradient caused by the fluid injection at the bottom, which is inversely proportional to the permeability (Eq. 10). Therefore, if a permeable layer is capped by a less permeable material, the large pressure gradient in the cap causes a significant pressure increase in the lower layer (Fig. 2a).

Equation (3) is simplified as

$$\frac{\partial T}{\partial t} = -V_T \frac{\partial T}{\partial z}, \tag{11}$$

assuming that $|V_T \partial T/\partial z| \gg |D_T \partial^2 T/\partial z^2|$. This approximation is likely true, as

$$\left| V_T \frac{\partial T}{\partial z} \right| \sim V_T \frac{T}{\delta}, \tag{12}$$

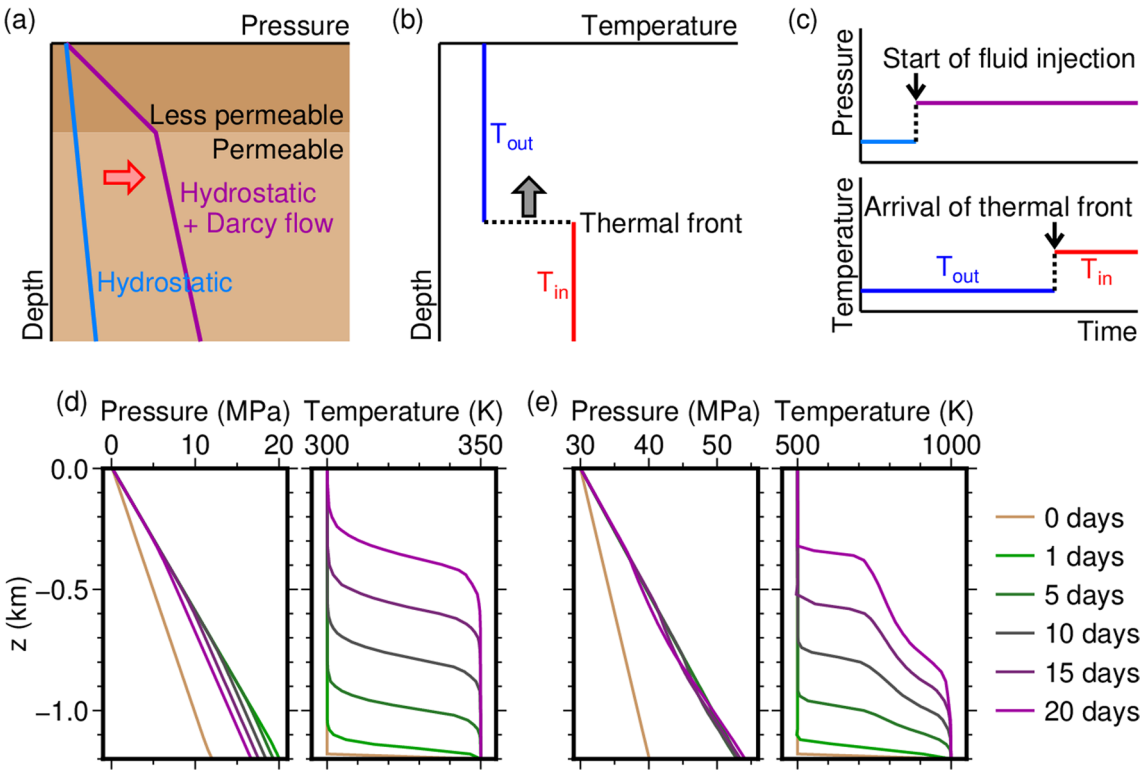

Fig. 2 Results of the one-dimensional model. **a** Analytical solutions for pressure and (**b**) temperature in the case of constant fluid properties. **c** Temporal variations. **d** Numerical solutions for pressure (left) and temperature (right) for fully liquid ($T_{out} = 300$ K, $P_{out} = 0.1$ MPa, $T_{in} = 350$ K, $V_{in} = 2.5 \times 10^{-4}$ m s^{-1}, and $k = 3 \times 10^{-11}$ m^2) and (**e**) supercritical scenarios ($T_{out} = 500$ K, $P_{out} = 30$ MPa, $T_{in} = 1000$ K, $V_{in} = 1 \times 10^{-3}$ m s^{-1}, and $k = 2 \times 10^{-12}$ m^2)

$$\left| D_T \frac{\partial^2 T}{\partial z^2} \right| \sim \frac{K_s}{\rho_s C_{ps}} \frac{T}{\delta^2} \left(for\ \phi \ll 1 \right), \tag{13}$$

and thus

$$V_T \frac{\partial T}{\partial z} \Big/ D_T \frac{\partial^2 T}{\partial z^2} \sim \frac{\rho_s C_{ps} V_T \delta}{K_s}, \tag{14}$$

where δ is a typical length scale of spatial temperature variation. Typical values of volcanic rocks (Eqs. 7–9) and a velocity consistent with the 27-day-long precursory period in 2014:

$$V_T \sim 1.2\,\mathrm{km} \Big/ 27\,\mathrm{day} \sim 5 \times 10^{-4} \mathrm{ms}^{-1}, \tag{15}$$

suggests that $|V_T \partial T/\partial z| > |D_T \partial^2 T/\partial z^2|$ if $\delta > 0.001$ m. Therefore, except for the case of an extremely small δ, Eq. (11) is a good first order approximation. It has a general solution

$$T(t,z) = f\left(t - \frac{z}{V_T} \right), \tag{16}$$

where f denotes an arbitrary function. Inserting the initial condition $T(0,z) = T_{out}$ $(z > -L)$ and the boundary condition at the bottom $T(t,-L) = T_{in}$ $(t > 0)$ into (16) yields

$$T(t,z) = \begin{cases} T_{out} & (z > -L + V_T t) \\ T_{in} & (z < -L + V_T t) \end{cases}. \tag{17}$$

This solution shows that low (initial)- and high (injected)-temperature regions are developed (Fig. 2b) rather than gradual heating over the entire region. Woods (2015) introduced this behavior based on an equation identical to Eq. (3) without explicitly providing its solution (Eq. 17). He explained this behaviour by a local thermal equilibrium between the fluid and porous matrix: the injected fluid heats the matrix to achieve equilibrium at a temperature T_{in} near the inlet, whereas the fluid that has lost heat is cooled to T_{out} to achieve equilibrium at locations far from the inlet. The boundary between the cold and hot regions, known as a thermal front (Woods 2015), propagates upward at a velocity V_T (Eq. 4), which is approximated as

$$V_T \sim \frac{\rho_f C_{pf}}{\rho_s C_{ps}} V = \frac{\rho_f C_{pf}}{\rho_s C_{ps}} V_{in} \tag{18}$$

in the case of a small porosity ($\phi \ll 1$). Inserting typical values of liquid water ($\rho_f \sim 1000$ kg m^{-3} and $C_{pf} \sim 4000$ J kg^{-1} K^{-1}; Wagner and Pruss 2002) and volcanic rocks (Eqs. 7–8) into Eq. (18) gives $V_T \sim 2V_{in}$ as a theoretical prediction for volcanic systems, while Woods (2015) argued that typically, $V_T \sim 1.1$–$1.2\ V_{in}$ for more widespread applications. In either case, V_T is a small factor larger than V_{in}.

Figure 2c shows the temporal changes in the pressure and temperature at an arbitrary underground site. Equation (10) has no time-dependent term, indicating that the pressure responds to V_{in} immediately (Fig. 2c, top). Equation (17) indicates that the temperature remains at its initial value until the thermal front reaches the observation point (Fig. 2c, bottom). A lag time is observed between the pressure and temperature changes (Fig. 2c).

1-D numerical model

The 1-D numerical model was examined for two sets of parameters: one that would result in the liquid state of water over the entire domain, and the other that would result in the presence of supercritical water. The first (fully liquid) scenario used $T_{out} = 300$ K, $P_{out} = 0.1$ MPa, and $T_{in} = 350$ K to avoid boiling. The purpose of this scenario was not to approximate an actual volcano but to examine the findings in the analytical model (Fig. 2a–c) under realistic fluid properties. The values of V_{in} and k were selected to fulfill the precursory time scale in 2014 (Eq. 15), keeping the pressure below the critical point of water ($P_c = 22.064$ MPa). Equations (15) and (18) reduce to:

$$V_{in} \sim \frac{\rho_s C_{ps}}{\rho_f C_{pf}} \times 5 \times 10^{-4} \mathrm{ms}^{-1}, \tag{19}$$

and Eq. (2) leads to:

$$k = -\mu_f V \left(\frac{\partial P}{\partial z} + \rho_f g \right)^{-1} \sim \mu_f V_{in} \left(\frac{P_{in} - P_{out}}{L} - \rho_f g \right)^{-1}, \tag{20}$$

where P_{in} is the pressure at the inlet. The values of ρ_f, C_{pf}, and μ_f for a given temperature and pressure were computed using the IAPWS-95 (Wagner and Pruss 2002; Huber et al. 2009). For any choice of temperature from T_{out} to T_{in} at a 1 K interval and pressure from P_{out} to P_c at a 0.1 MPa interval, V_{in} and k from Eqs. (19) and (20) were within 2.4–2.5×10^{-4} m s^{-1} and 1.0–2.5×10^{-11} m^2, respectively, in the case of $P_{in} = P_c$. For the pressure to be subcritical ($P_{in} < P_c$), k must be greater than this range (Eq. 20). Therefore, the simulation used $V_{in} = 2.5 \times 10^{-4}$ m s^{-1} and $k = 3 \times 10^{-11}$ m^2. The results (Fig. 2d) show that the pressure increased within 1 day in response to the fluid injection, and a sharp thermal front propagated upward at a velocity close to the expected value (Eq. 15). These results show that the behavior of the fully liquid system is well approximated by the analytical solution.

The second (supercritical) scenario used $T_{out} = 500$ K, $P_{out} = 30$ MPa, and $T_{in} = 1000$ K. Appropriate values of V_{in} and k were determined using the same strategy as the liquid scenario, except that $P_{in} = 50$ MPa (which gave a pressure difference $P_{in} - P_{out}$ close to that of the liquid scenario) was used and Eqs. (19) and (20) were evaluated for pressures from P_{out} to P_{in}. The results were 0.1–5.1 $\times 10^{-3}$ m s^{-1} for V_{in} and 0.3–12.7 $\times 10^{-12}$ m^2 for k; they varied largely because of large variations in fluid properties. Trial simulations were performed with several values of V_{in} and k, and the results were similar, except for different time scales and pressure change amplitudes. Figure 2e shows the results from $V_{in} = 1 \times 10^{-3}$ m s^{-1} and $k = 2 \times 10^{-12}$ m^2, which exhibited a time scale and pressure change amplitude close to those of the fully liquid scenario. The major difference in the results from the two scenarios was a broader transition zone of the temperature in the supercritical case (Fig. 2e) than in the fully liquid case (Fig. 2d). This was probably because V_T was smaller at higher temperatures due to the smaller ρ_f in Eq. (18). The temperature distribution bent near 700 K (Fig. 2e) because of a large C_{pf}, and thus a large V_T (Eq. 18).

2-D model

Two scenarios were examined for the 2-D model (Fig. 1b): one with a relatively low temperature $T_{in} = 600$ K for reproducing the time sequence in 2014 and the other with a higher temperature $T_{in} = 800$ K for 2007. The temperatures were not constrained by field observations; however, the assumption of a higher temperature in 2007 than in 2014 was reasonable given the distinct preeruptive crustal deformation in 2007, which was interpreted as magma intrusion (Nakamichi et al. 2009; Takagi and Onizawa 2016; Murase et al. 2016), and its absence in 2014 (Miyaoka and Takagi 2016).

Figure 3a shows an example of the computation results, where the spatiotemporal distribution of the pressure, temperature, and specific volume are shown. The pressure in the channel increased within 1 day, similar to the 1-D result (Fig. 2). The thermal front migrated upward and reached the OED–basement boundary at ~ 20 days. The vapor phase occurred for the first time at 29 days and at 1 km asl., consistent with the time sequence in 2014.

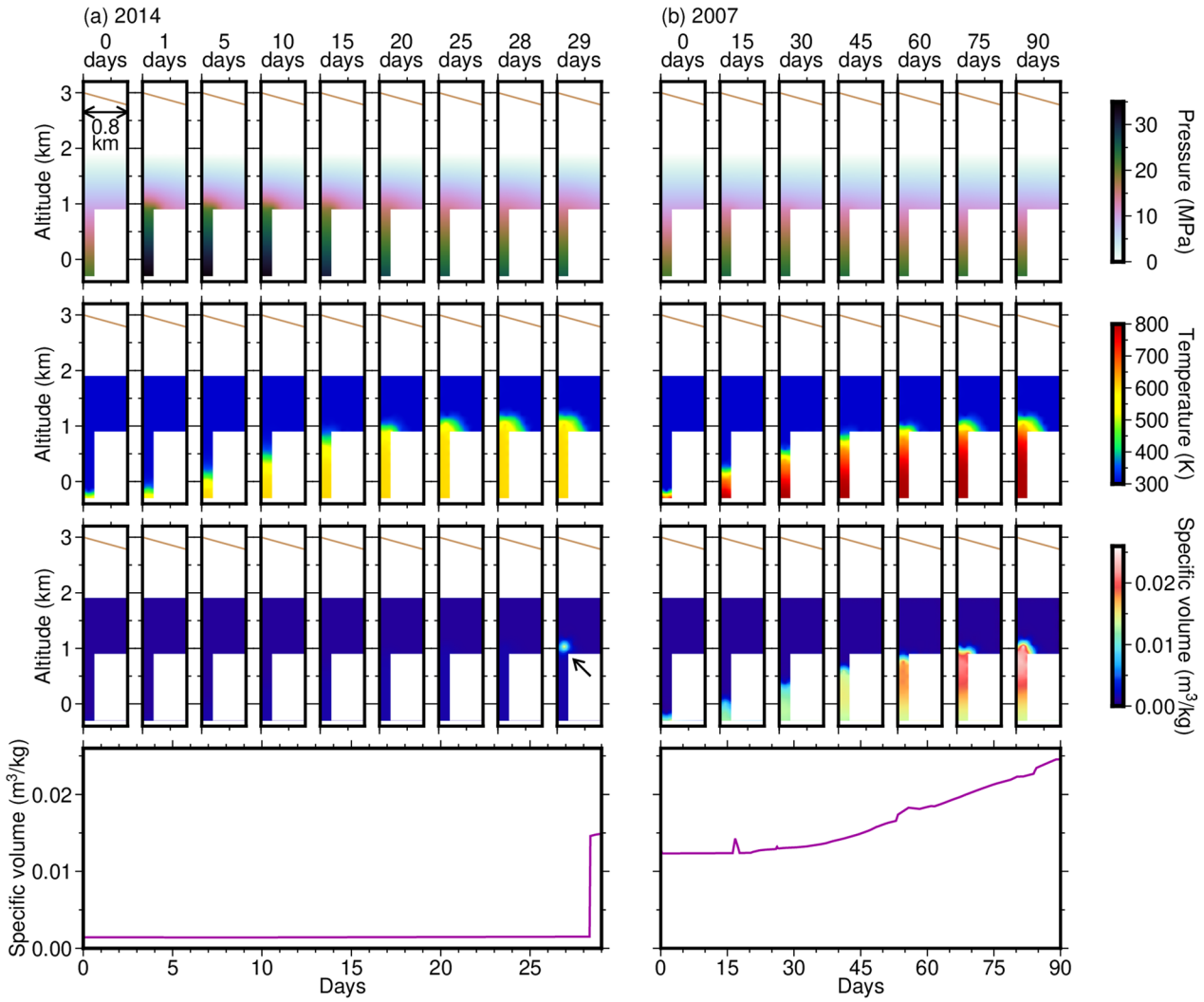

Fig. 3 Simulation results of two-dimensional models for (**a**) 2014 and (**b**) 2007 scenarios. The upper three panels show the pressure, temperature, and specific volume of water at selected time samples. The bottom panels show the temporal variation of the maximum value of the specific volume of water at a 1-h temporal resolution

Vaporization was simply the result of the pressure and temperature that reached the boiling condition of water; microscopic details of the vaporization process were not incorporated in the numerical model.

The simulation in Fig. 3a used $V_{in} = 6 \times 10^{-4}$ m s^{-1}, $k_o = 4 \times 10^{-12}$ m^2, $k_c = 100k_o$, $\phi_o = 0.05$, $\phi_c = 0.2$, and $\alpha_B = 0.4$. This study constrained these parameters based on a comparison of the simulation results with the observed 2014 precursory sequence; no independent information was available to constrain them. Therefore, the parameters should not be viewed as a petrologically reasonable choice but as the result of the optimization of unknown model parameters. The simulation results were most sensitive to V_{in} and k_o. Figure 4a shows the number of days to the first occurrence of vaporization in the 2014 scenario evaluated from the pressure and temperature at each location and time step. This time length was interpreted as a precursory VT seismicity period, assuming that a pore-fluid pressure increase, which occurred at < 1 day, activated the seismicity, whereas the vaporization resulted in an eruption. The modeled and actual (25–30 days) precursory periods were consistent for several choices of V_{in} and k_o (Fig. 4a, bold; requirement 1). Increasing (decreasing) the inflow velocity (V_{in}) or the permeability of the OED (k_o) resulted in a shorter (longer) modeled precursory period than the actual period, which provided constraints for V_{in} and k_o. Figure 4b shows the location of the first vaporization. An acceptable range for the location (bold; requirement 2) was between the bottom of the OED (0.9 km asl.), which likely acted as

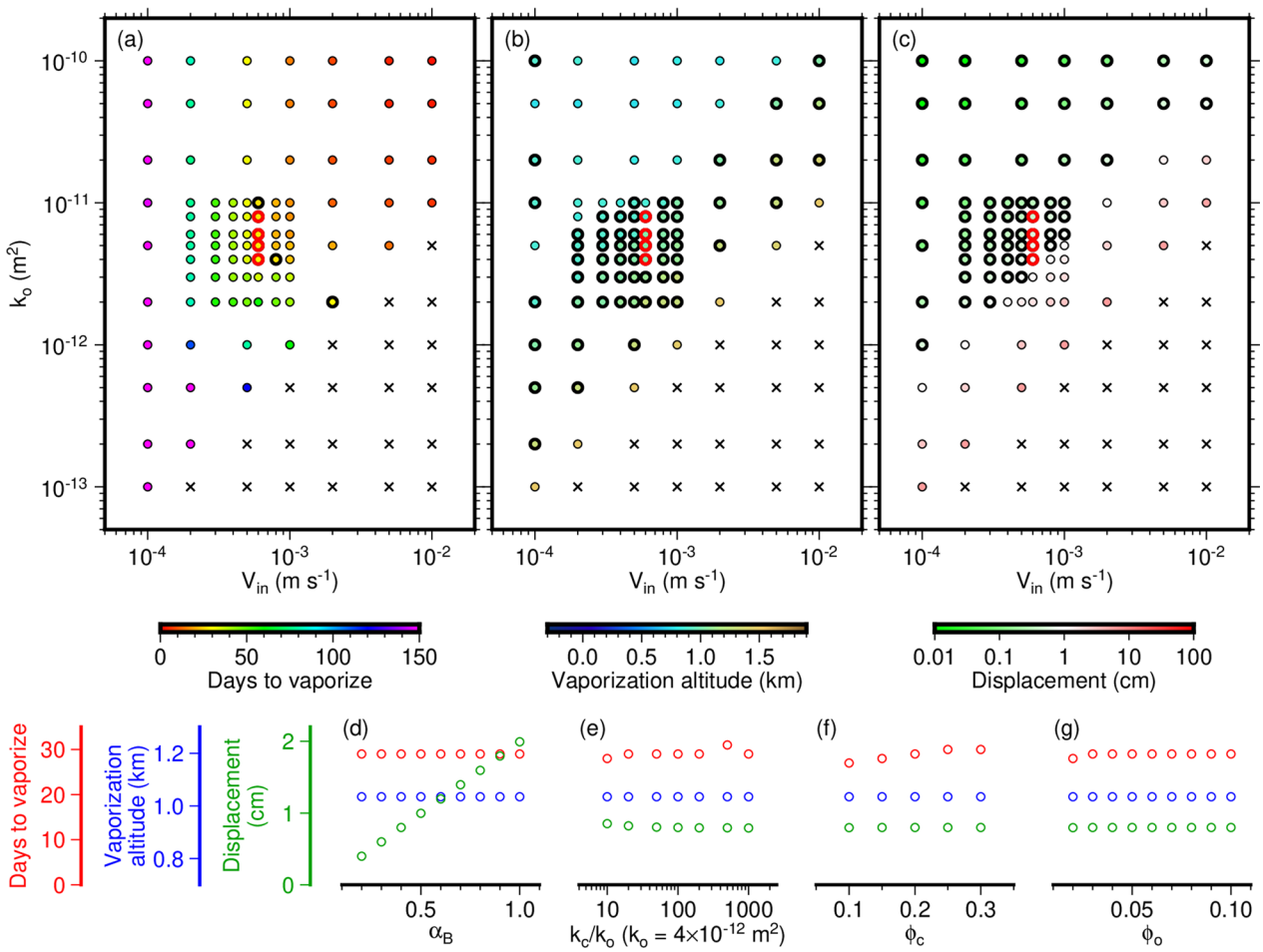

Fig. 4 Parameter dependence of the two-dimensional model for the 2014 scenario. One or two parameters were varied in each panel, fixing the other parameters as $V_{in} = 6 \times 10^{-4}$ m s^{-1}, $k_o = 4 \times 10^{-12}$ m.^{2}, $\alpha_B = 0.4$, $k_c = 100k_o$, $\phi_c = 0.2$, and $\phi_o = 0.05$. The number of days to the first vaporization (**a** and red in **d**–**g**), the altitude of the vaporization (**b** and blue in **d**–**g**), and the maximum ground surface displacement (**c** and green in **d**–**g**) are shown. Bold circles show acceptable ranges: 25–30 days in (**a**), 0.9–1.4 km above sea level in (**b**), and < 1 cm in (**c**); the three requirements are satisfied for the circles with red boundaries. Crosses represent failed computations due to a pressure outside the valid range of IF-97

a barrier beforehand and was broken during the 2014 eruption (Maeda et al. 2017; Maeda and Watanabe 2023), and the centroid of the source of a tilt change (1.4 km asl.) that immediately preceded the eruption (Maeda et al. 2017). Figure 4c shows the maximum ground surface displacement. Given little precursory deformation in 2014, the displacement was likely less than 1 cm (Fig. 4c, bold; requirement 3), which is a typical detection limit of the Global Navigation Satellite System (GNSS) and interferometric synthetic aperture radar (InSAR) observations. The ground surface displacement is related to the magnitude of the pressure change. A larger V_{in} or smaller k_o resulted in a larger pressure change (Eq. 10), and thus, a larger ground surface displacement (Fig. 4c). The requirements 1–3 were simultaneously satisfied for $V_{in} = 6 \times 10^{-4}$ m s^{-1} and $k_o = 4$–8×10^{-12} m^2 (Fig. 4a–c, red bounds). This study selected the lowest permeability among them ($k_o = 4 \times 10^{-12}$ m^2) because it was used for a low-permeability OED layer. Although this permeability was relatively high, it was within the range of permeabilities measured (10^{-11}–10^{-19} m^2; Heap et al. 2017) or considered in an independent numerical model (10^{-10}–10^{-13} m^2; Tanaka et al. 2018) for other volcanoes. Smaller permeabilities could not explain the precursory period (Fig. 4a) or the ground surface displacement (Fig. 4c). The choice of the other parameters had little effect on the fluid and heat flows (Fig. 4d–g, red and blue), although α_B, which could be between the porosity of the medium (for a stiff material) and 1 (for a soft material; COMSOL

1998–2022b), controlled the magnitude of the crustal deformation(Fig. 4d, green).

The simulation for 2007 used $T_{in} = 800$ K. Several values of V_{in} were tested, and the result from $V_{in} = 1.2 \times 10^{-3}$ m s^{-1} is shown here, which exhibited a time scale similar to that of the 2007 precursory sequence. The other parameters were unchanged from the 2014 scenario. The results (Fig. 3b) are characterized by a gradual increase in the specific volume. This is because a supercritical state occurred in deep parts at a relatively early stage. A phase change from liquid to gas caused a discontinuity in the density and thus in the specific volume, while phase changes from liquid to supercritical and from supercritical to gas were 2nd-order phase transitions that did not involve a discontinuity in the density or volume.

The results were not perfectly stable, as shown by the small fluctuations in Fig. 4e (red) and the unnatural short-lived transients in the maximum specific volume in Fig. 3b (e.g., near 17 days). However, the instability did not grow with time and disappeared after a short period of time (Fig. 3b), suggesting that the outline of the result was not significantly affected by instability.

Discussion and conclusions

A feature commonly present in all results was an immediate pressure increase over the entire region in response to fluid injection (Figs. 2 and 3). The time scale of the pressure increase (<1 day) was faster than that expected from the speed of fluid migration. For example, $V_{in} = 2.5 \times 10^{-4}$ m s^{-1} was used in Fig. 2d, suggesting that the fluid reached the top of the channel after $L/V_{in} = 4.8 \times 10^{6}$ s (~56 days). Nevertheless, the pressure increased within 1 day, even near the top of the channel (Fig. 2d). A key to understanding this behavior is the existing fluid in the porous medium. When a new fluid is injected into the medium, the existing fluid is either compressed or pushed away, resulting in a pressure increase even at sites apart from the inlet. The existing fluid is also a key to understanding Fig. 4. The permeability of the least permeable OED layer (k_o) significantly affected the results (Fig. 4a–c), whereas that of the permeable channel (k_c) did not (Fig. 4e), suggesting that the ability for the existing fluid to flow controlled the entire process.

The temperature was separated into cold and hot regions, with a narrow transition zone in the case of liquid (Figs. 2b and d) and a relatively broad zone in the case of supercritical water (Fig. 2e). The 2014 scenario (Fig. 3a) resembled the fully liquid case because the injected fluid

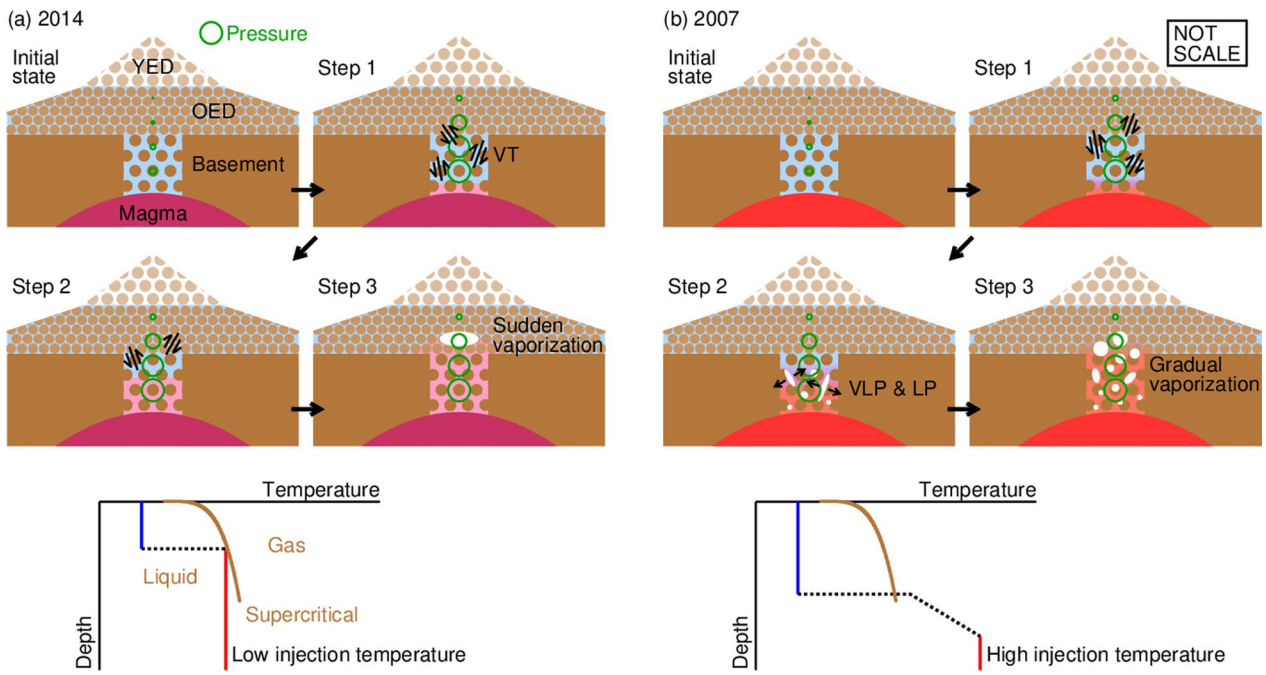

Fig. 5 Schematic illustrations of (**a**) 2014 and (**b**) 2007 scenarios. The horizontal scales of the surface topography and permeable channel are compressed and extended, respectively, from their actual dimensions for illustration

temperature ($T_{in} = 600$ K) was lower than the critical temperature of water ($T_c = 647.096$ K). Figure 5a explains this result. Water was liquid over the entire region when the thermal front was deep (Fig. 5a, steps 1 and 2). When the thermal front reached a shallow part and intersected the boiling curve (Fig. 5a, bottom), a sudden vaporization of liquid water (Fig. 5a, step 3) caused a violent phreatic eruption. In the 2007 scenario (Fig. 3b), where $T_{in} = 800$ K $> T_c$, the heated water in the deep parts was in a supercritical state (Fig. 5b, bottom), resulting in a gradual increase in the volume of fluid (Fig. 3b).

These features may explain the precursory time sequences of the 2007 and 2014 eruptions. The pressurized fluid immediately activated VT seismicity in 2007 and 2014 (Fig. 2c; step 1 of Fig. 5). The magnitude of the modeled pore-fluid pressure change was ~ 10 MPa (Fig. 3), which is close to that estimated as a trigger for seismic swarms in the base region of Mt. Ontake (Terakawa 2017) and several other regions (De Matteis et al. 2021; Nakagomi et al. 2021). Keranen et al. (2014, and references therein) suggests that a pressure change of 0.01–0.1 MPa is sufficient for an earthquake trigger if the faults are near failure. This pressure change is likely too small to trigger VT seismicity at Mt. Ontake because little seismicity before the 2007 and 2014 precursory periods suggests that the summit region of Mt. Ontake was not near failure. Amezawa et al. (2023) estimated a pressure change of ~ 100 MPa as a trigger for earthquakes between 2018 and 2022 in Noto, Japan, at 10–15 km depths. The focal depths of ~ 2 km for the VT seismicity of Mt. Ontake (Fig. 1b) suggest a smaller rock strength, and thus a smaller pressure change needed to trigger earthquakes, than Noto. From these points, a pressure change of ~ 10 MPa (Fig. 3) is considered to be a reasonable magnitude for triggering VT seismicity at Mt. Ontake.

In 2007, the volume increase of water from liquid to supercritical and then to gas states (Fig. 3b) caused VLP and LP seismicity and tremors (Fig. 5b, step 2). These signals are widely observed at volcanoes and are attributed to fluid–rock interactions (Chouet and Matoza 2013). In general, the source mechanisms of seismic events consist of double-couple, compensated linear vector dipole (CLVD), and isotropic (volumetric change) components. Waveform inversion of VLP events at Mt. Ontake (Nakamichi et al. 2009; Maeda et al. 2015) and other volcanoes (Konstantinou 2023, and references therein) show that the isotropic component is dominant. Several studies have demonstrated that LP events (e.g., Nakano et al. 2003; De Barros et al. 2011; Matoza et al. 2015) and tremors (Davi et al. 2012) are also associated with the isotropic mechanism, although the source mechanisms in the LP band are generally difficult to estimate (Bean et al. 2008). Few VLP and LP events and tremors before the 2014 eruption may be due to the fully liquid water (Fig. 5a, steps 1 and 2); the small compressibility of the liquid phase limits the magnitude of volumetric changes. Despite the few precursors, the eruption was larger in 2014 because of the abrupt volume increase from liquid to vapor (Figs. 3a and 5a) than in 2007 when the volume of fluid increased gradually (Figs. 3b and 5b).

Future tasks include estimating the source mechanisms of LP events and tremors at Mt. Ontake. A liquid phase could interact with rocks to generate signals similar to LP events and tremors; in this case, the mechanism would be dominantly CLVD rather than the isotropic component because the liquid has a small compressibility. This study assumed that LP events and tremors occur mainly by volumetric changes and therefore by compressible gas or supercritical fluids. The validity of this assumption needs to be examined from seismic data. Another task is to constrain the unknown parameters in the model, including the porosities and permeabilities in each layer and the initial temperature distribution. Ikehata and Maruoka (2016) found that the temperatures of the ejected materials were 543–554 K before the 2014 eruption. Therefore, the initial temperature near the eruption source should be ~ 550 K, whereas this study assumed a uniform temperature of 300 K for the initial condition because there was no information to constrain the spatial distribution of the temperature. Permeability must also be estimated independently. These are the main points to be examined and improved upon in future studies.

Supplementary Information

The online version contains supplementary material available at https://doi.org/10.1186/s40623-024-02013-8.

Additional file 1. Exact steps and parameters used in the simulations.

Acknowledgements

Comments by Nico Fournier and an anonymous reviewer helped to improve the manuscript. This work was supported by JSPS KAKENHI Grant Number JP19K04016.

Author contributions

YM conducted the simulations and drafted the manuscript.

Funding

* JSPS KAKENHI Grant Number JP19K04016.

Availability of data and materials

The numerical procedures and parameters are fully described in Additional file 1. Following this, anyone who has a license for COMSOL Multiphysics (including appropriate option modules) can exactly reproduce the computations presented in this paper.

Declarations

Competing interests

The authors declare that they have no competing interests.

Author details
[1]Graduate School of Environmental Studies, Nagoya University, D2-2 (510) Furo-Cho, Chikusa-Ku, Nagoya, Aichi 464-8601, Japan.

Received: 28 November 2023 Accepted: 17 April 2024
Published online: 01 May 2024

References

Amezawa Y, Hiramatsu Y, Miyakawa A, Imanishi K, Otsubo M (2023) Long-living earthquake swarm and intermittent seismicity in the northeastern tip of the Noto Peninsula Japan. Geophys Res Lett 50:e20221GL02670. https://doi.org/10.1029/2022GL102670

Arens F, Coco A, Gottsmann J, Hickey J, Kilgour G (2022) Multiphysics modeling of volcanic unrest at Mt. Ruapehu (New Zealand). Geochemi Geophys Geosys 23:e202201GC0572. https://doi.org/10.1029/2022GC010572

Asai K, Satake H, Tsujimura M (2006) Characteristics of groundwater flow in Ontake stratovolcano, central Japan, with reference to erosion conditions. J Groundwater Hydrol 48(4):279–296. https://doi.org/10.5917/jagh1987.48.279

Bean C, Lokmer I, O'Brien G (2008) Influence of near-surface volcanic structure on long-period seismic signals and on moment tensor inversions: Simulated examples from Mount Etna. J Geophys Res 113:B08308. https://doi.org/10.1029/2007JB005468

Chouet BA, Matoza RS (2013) A multi-decadal view of seismic methods for detecting precursors of magma movement and eruption. J Volcanol Geotherm Res 252:108–175. https://doi.org/10.1016/j.jvolgeores.2012.11.013

COMSOL (1998–2022a) Chemical reaction engineering module user's guide ver: COMSOL 6.1. https://doc.comsol.com/6.1/docserver/

COMSOL (1998–2022b) Porous media flow module user's guide ver: COMSOL 6.1. https://doc.comsol.com/6.1/docserver/

Davi R, O'Brien GS, De Barros L, Lokmer I, Bean CJ, Lesage P, Mora MM, Soto GJ (2012) Seismic source mechanisms of tremor recorded on Arenal volcano, Costa Rica, retrieved by waveform inversion. J Volcanol Geotherm Res 213–214:1–13. https://doi.org/10.1016/j.jvolgeores.2011.10.008

De Barros L, Lokmer I, Bean CJ, O'Brien GS, Saccorotti G, Métaxian J-P, Zuccarello L, Patanè D (2011) Source mechanism of long-period events recorded by a high-density seismic network during the 2008 eruption on Mount Etna. J Geophys Res 116:B01304. https://doi.org/10.1029/2010JB007629

De Matteis R, Convertito V, Napolitano F, Amoroso O, Terakawa T, Capuano P (2021) Pore fluid pressure imaging of the Mt. Pollino region (southern Italy) from earthquake focal mechanisms. Geophys Res Lett 48:e2021GL094552. https://doi.org/10.1029/2021GL094552

Heap MJ, Kennedy BM, Farquharson JI, Ashworth J, Mayer K, Letham-Brake M, Reuschlé T, Gilg HA, Scheu B, Lavallée Y, Siratovich P, Cole J, Jolly AD, Baud P, Dingwell DB (2017) A multidisciplinary approach to quantify the permeability of the Whakaari/White Island volcanic hydrothermal system (Taupo Volcanic Zone, New Zealand). J Volcanol Geotherm Res 332:88–108. https://doi.org/10.1016/j.jvolgeores.2016.12.004

Heap MJ, Kushnir ARL, Vasseur J, Wadsworth FB, Harlé P, Baud P, Kennedy BM, Troll VR, Deegan FM (2020) The thermal properties of porous andesite. J Volcanol Geotherm Res 398:106901. https://doi.org/10.1016/j.jvolgeores.2020.106901

Huber ML, Perkins RA, Laesecke A, Friend DG, Sengers JV, Assael MJ, Metaxa IN, Vogel E, Mares R, Miyagawa K (2009) New international formulation for the viscosity of H2O. J Phys Chem Ref Data 38(2):101–125. https://doi.org/10.1063/1.3088050

Ikehata K, Maruoka T (2016) Sulfur isotopic characteristics of volcanic products from the September 2014 Mount Ontake eruption Japan. Earth Planets Space 68:116. https://doi.org/10.1186/s40623-016-0496-z

Japan Meteorological Agency (2007) Annual volcanic activity report of Ontakesan. https://www.data.jma.go.jp/svd/vois/data/tokyo/STOCK/monthly_v-act_doc/monthly_vact_vol.php?id=312. Accessed 22 Nov 2023

Japan Meteorological Agency (2014) Annual volcanic activity report of Ontakesan. https://www.data.jma.go.jp/svd/vois/data/tokyo/STOCK/monthly_v-act_doc/monthly_vact_vol.php?id=312. Accessed 22 Nov 2023

Kato A, Terakawa T, Yamanaka Y, Maeda Y, Horikawa S, Matsuhiro K, Okuda T (2015) Preparatory and precursory processes leading up to the 2014 phreatic eruption of Mount Ontake Japan. Earth Planets Space 67:111. https://doi.org/10.1186/s40623-015-0288-x

Keranen KM, Weingarten M, Abers GA, Bekins BA, Ge S (2014) Sharp increase in central Oklahoma seismicity since 2008 induced by massive wastewater injection. Science 345:448–451. https://doi.org/10.1126/science.1255802

Konstantinou KI (2023) A review of the source characteristics and physical mechanisms of very long period (VLP) seismic signals at active volcanoes. Surv Geophys. https://doi.org/10.1007/s10712-023-09800-0

Maeda Y, Watanabe T (2023) Seismic structure and its implication on the hydrothermal system beneath Mt. Ontake, central Japan. Earth Planets Space 75:115. https://doi.org/10.1186/s40623-023-01870-z

Maeda Y, Kato A, Terakawa T, Yamanaka Y, Horikawa S, Matsuhiro K, Okuda T (2015) Source mechanism of a VLP event immediately before the 2014 eruption of Mt. Ontake Japan. Earth Planets Space 67:187. https://doi.org/10.1186/s40623-015-0358-0

Maeda Y, Kato A, Yamanaka Y (2017) Modeling the dynamics of a phreatic eruption based on a tilt observation: barrier breakage leading to the 2014 eruption of Mount Ontake Japan. J Geophys Res Solid Earth 122(2):1007–1024. https://doi.org/10.1002/2016JB013739

Maeno F, Nakada S, Oikawa T, Yoshimoto M, Komori J, Ishizuka Y, Takeshita Y, Shimano T, Kaneko T, Nagai M (2016) Reconstruction of a phreatic eruption on 27 September 2014 at Ontake volcano, central Japan, based on proximal pyroclastic density current and fallout deposits. Earth Planets Space 68:82. https://doi.org/10.1186/s40623-016-0449-6

Matoza RS, Chouet BA, Dawson PB, Shearer PM, Haney MM, Waite GP, Moran SC, Mikesell TD (2015) Source mechanism of small long-period events at Mount St. Helens in July 2005 using template matching, phase-weighted stacking, and full-waveform inversion. J Geophys Res Solid Earth 120:6351–6364. https://doi.org/10.1002/2015JB012279

Miyagi I, Geshi N, Hamasaki S, Oikawa T, Tomiya A (2020) Heat source of the 2014 phreatic eruption of Mount Ontake Japan. Bull Volcanol 82:33. https://doi.org/10.1007/s00445-020-1358-x

Miyaoka K, Takagi A (2016) Detection of crustal deformation prior to the 2014 Mt. Ontake eruption by the stacking method. Earth Planets Space 68:60. https://doi.org/10.1186/s40623-016-0439-8

Murase M, Kimata F, Yamanaka Y, Horikawa S, Matsuhiro K, Matsushima T, Mori H, Ohkura T, Yoshikawa S, Miyajima R, Inoue H, Mishima T, Sonoda T, Uchida K, Yamamoto K, Nakamichi H (2016) Preparatory process preceding the 2014 eruption of Mount Ontake volcano, Japan: insights from precise leveling measurements. Earth Planets Space 68:9. https://doi.org/10.1186/s40623-016-0386-4

Nakagomi K, Terakawa T, Matsumoto S, Horikawa S (2021) Stress and pore fluid pressure control of seismicity rate changes following the 2016 Kumamoto earthquake Japan. Earth Planets Space 73:11. https://doi.org/10.1186/s40623-020-01329-5

Nakamichi H, Kumagai H, Nakano M, Okubo M, Kimata F, Ito Y, Obara K (2009) Source mechanism of a very-long-period event at Mt Ontake, central Japan: response of a hydrothermal system to magma intrusion beneath the summit. J Volcanol Geotherm Res 187(3–4):167–177. https://doi.org/10.1016/j.jvolgeores.2009.09.006

Nakano M, Kumagai H, Chouet BA (2003) Source mechanism of long-period events at Kusatsu-Shirane Volcano, Japan, inferred from waveform inversion of the effective excitation functions. J Volcanol Geotherm Res 122(3–4):149–164. https://doi.org/10.1016/S0377-0273(02)00499-7

Newhall CG, Self S (1982) The volcanic explosivity index (VEI): an estimate of explosive magnitude for historical volcanism. J Geophys Res 87(C2):1231–1238. https://doi.org/10.1029/JC087iC02p01231

Ogiso M, Matsubayashi H, Yamamoto T (2015) Descent of tremor source locations before the 2014 phreatic eruption of Ontake volcano Japan. Earth Planets Space 67:206. https://doi.org/10.1186/s40623-015-0376-y

Oikawa T, Yoshimoto M, Nakada S, Maeno F, Komori J, Shimano T, Takeshita Y, Ishizuka Y, Ishimine Y (2016) Reconstruction of the 2014 eruption sequence of Ontake Volcano from recorded images and interviews. Earth Planets Space 68:79. https://doi.org/10.1186/s40623-016-0458-5

Sano Y, Kagoshima T, Takahata N, Nishio Y, Roulleau PDL, Fischer TP (2015) Ten-year helium anomaly prior to the 2014 Mt Ontake eruption. Sci Rep 5:13069. https://doi.org/10.1038/srep13069

Stissi SC, Napoli R, Currenti G, Afanasyev A, Montegrossi G (2021) Influence of permeability on the hydrothermal system at Vulcano Island (Italy):

inferences from numerical simulations. Earth Planets Space 73:179. https://doi.org/10.1186/s40623-021-01515-z
Takagi A, Onizawa S (2016) Shallow pressure sources associated with the 2007 and 2014 phreatic eruptions of Mt. Ontake Japan. Earth Planets Space 68:135. https://doi.org/10.1186/s40623-016-0515-0
Tanaka R, Hashimoto T, Matsushima N, Ishido T (2018) Contention between supply of hydrothermal fluid and conduit obstruction: inferences from numerical simulations. Earth Planets Space 70:72. https://doi.org/10.1186/s40623-018-0840-6
Terakawa T (2017) Overpressurized fluids drive microseismic swarm activity around Mt. Ontake volcano Japan. Earth Planets Space 69:87. https://doi.org/10.1186/s40623-017-0671-x
Terakawa T, Kato A, Yamanaka Y, Maeda Y, Horikawa S, Matsuhiro K, Okuda T (2016) Monitoring eruption activity using temporal stress changes at Mount Ontake volcano. Nat Commun 7:10797. https://doi.org/10.1038/ncomms10797
Tsunematsu K, Ishimine Y, Kaneko T, Yoshimoto M, Fujii T, Yamaoka K (2016) Estimation of ballistic block landing energy during 2014 Mount Ontake eruption. Earth Planets Space 68:88. https://doi.org/10.1186/s40623-016-0463-8
Wagner W, Pruss A (2002) The IAPWS formulation 1995 for the thermodynamic properties of ordinary water substance for general and scientific use. J Phys Chem Ref Data 31(2):387–535. https://doi.org/10.1063/1.1461829
Woods AW (2015) Flow in porous rocks—energy and environmental applications. Cambridge University Press, Cambridge. https://doi.org/10.1017/CBO9781107588677

Publisher's Note